Communication

Fully-Metallic 3-D Cells for Wideband Applications

M. A. Balmaseda-Márquez, S. Moreno-Rodríguez, P. H. Zapata, C. Molero, and J. F. Valenzuela-Valdés

***Abstract*— This communication presents a novel full-metal 3-D periodic structure that allows for the excitation of phase resonance. This phenomenon, thanks to the 3-D geometry, enables the individual control of the phase response of each polarization along the frequency band. This structure is inspired by square waveguides that have open resonators slotted on the walls. An extended study has been carried out by modeling the unit cell via equivalent circuits with the goal of developing a powerful optimization tool instead of using more resource-consuming software. An ultrawideband electric-field rotator covering a bandwidth of 141.8% has been designed with the aid of the circuit model (CM) and has been manufactured via 3-D-printing laser powder bed fusion (LPBF). The experimental results have been validated with success.**

***Index Terms*— 3-D fully-metallic cells, circuit models (CMs), polarization conversion, wideband devices.**

I. Introduction

The permanent increase in the frequency for current functionalities in communication environments has always been a constant, forced by the tightening of performance requirements in terms of data rates and bandwidth capabilities [1]. Polarization-state topic in electromagnetic waves is not immune to the frequency increase, since more accuracy in terminals alignment and robustness in the generation is required [2], [3]. Polarization is a fundamental property of electromagnetic waves. Especially, linear-to-linear (90° rotation) becomes crucial in many application fields, such as millimeter imaging and detection, radar cross-section (RCS) reduction [5], [6], [7], or THz and infrared applications [8], [9], among others. Field rotation and polarization control have classically obtained by birefringent structures [10], or via classical grating screens [11], [12], where a nonnegligible percentage of the incident power gets lost. The recent improvements in the design of frequency-selective surfaces (FSSs) and metasurfaces have contributed to the development of more efficient designs of field rotators, with enhanced phase control, low profile, low weight, and low-cost [13], [14].

Most metasurfaces converting polarization are based on periodic or quasi-periodic 2-D distributions of scatterers printed on grounded dielectric substrates [15]. A sort of anisotropy or symmetry breaking is always provoked by the scatterer shapes [16]. Some well-known cases are those having diagonal symmetry [17], [18], [19], highly demanded in wideband applications. Chiral scatterers are also employed in the models in [27] and [21]. Generally, the 2-D character of all of these structures prevents an independent control of different field polarizations, demanding a compromise in the solution.

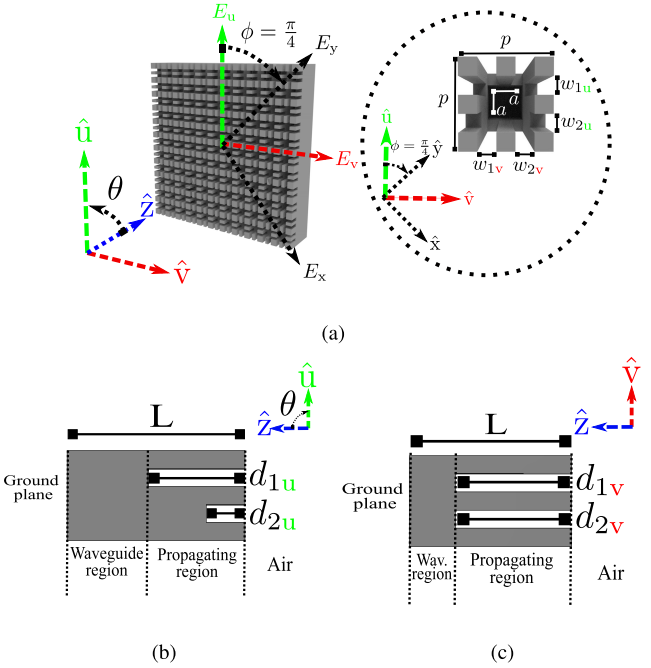

Fig. 1. 11 × 11-array in perspective and cell with the corresponding structure parameters. (a) Complete structure and front view of the cell. (b) Lateral view, parallel to the $\hat{\mathbf{u}}$-component. (c) Top view, parallel to the $\hat{\mathbf{v}}$-component.

It has been proven that a cleaner manipulation of different polarizations can be realized using 3-D metasurfaces [22]. Recent and impressive advances in 3-D printing techniques [23], [24] have brought the conception of novel 3-D terminals with exotic shapes and with a higher degree of versatility [25], [26]. Most of these new models can be fabricated in one piece, gaining mechanical robustness and self-sustainability. A very important property of 3-D cells is their inherent skill to control two different polarizations in a context of full independence [27], [28]. This property allows for accurate and individual control of the phase of orthogonal fields [29], [30]. In this sense, 3-D-printed metasurfaces become an attractive alternative to become a new generation of polarization converters/controllers [31]. Full-metal devices are recommended, for instance, in special scenarios where dielectric materials strongly suffer from extreme environmental conditions [32].

This communication is intended to describe the guidelines to design polarizers by using full-metal 3-D cells, particularly, an ultrawideband field rotator. The structure, illustrated in Fig. 1(a), is conceived to operate by inducing a known resonant principle: the so-called phase resonance [33], [34], manifested as a typical electric resonance [35], [36], [37]. The structure geometry is innovative since several slits are etched per wall, inducing complex phenomenology. A circuit model (CM) is proposed and numerically estimated, which provides a better understanding of cell behavior. The role of the

Manuscript received 23 December 2022; revised 3 February 2023; accepted 6 February 2023. Date of publication 3 March 2023; date of current version 5 May 2023. This work was supported in part by the Spanish Government under Project PID2020-112545RB-C54, Project TED2021-129938B-I, and ProjectPDC2022-133900-I00; in part by the "Junta de Andalucía" under Project A-TIC-608-UGR20 and Project P18.RT.4830; and in part by the Banco Bilbao Vizcaya Argentaria (BBVA) Foundation through the Project 2021 Leonardo Grant for Researchers and Cultural Creators. *(Corresponding author: C. Molero.)*

M. A. Balmaseda-Marquez, S. Moreno-Rodriguez, C. Molero, and J. F. Valenzuela-Valdes are with the Department of Signal Theory, Telematics and Communications, University of Granada, 18071 Granada, Spain (e-mail: cmoleroj@ugr.es).

P. H. Zapata is with the Department of Electrical and Computer Engineering, Aristotle University of Thessaloniki, 54124 Thessaloniki, Greece.

Color versions of one or more figures in this communication are available at https://doi.org/10.1109/TAP.2023.3249838.

Digital Object Identifier 10.1109/TAP.2023.3249838

slits is well represented by stubs [38]. The presence of multiple slit (stubs) per wall may induce mutual resonances between different stubs, manifesting as a sudden 180-phase shift [39]. By tuning the stub's dimensions, the position of these phase shifts can be moved in frequency. The CM is proven to be a very efficient design tool. A final design is presented, fabricated, and evaluated, showing a polarization conversion ratio (PCR) bandwidth of 141%. Finally, the novelties of the cell will be studied along the communication, emphasizing its full-metal 3-D nature (causing huge bandwidth capabilities), the multislit geometry, and the subsequent phase-resonance excitation as a potential element for designing purposes.

II. Cell Definition and Characterization

The unit cell under consideration in this communication is a classical waveguide with homogeneous slit perforations on the walls. Several perspectives of the cell are shown in Fig. 1. Two different waveguide sections can be identified: on the one hand, the section containing the slits, being the *propagating region*. For the sake of simplicity, only two slits are considered, but the number of slits is not restricted. On the other hand, the *waveguide region*, where the dominant field is described by the TE_{10} mode. This mode appears in evanescent nature, thanks to the small cell dimensions in comparison with the smallest operation wavelength λ_h ($a < \lambda_\mathrm{h}/2$). The waveguide region is terminated in the ground plane, forcing a full-reflection operation. It is worth remarking that the presence of this ground plane, the existence of a propagating region, and the multislit architecture make this cell novel and original.

The structure is excited by the incidence of a plane wave. The electric-field vector of this wave vibrates along the $\hat{\mathbf{y}}$-direction. Rigorously speaking, the electric-field vector can be decomposed into the components forming the principal axis of the cell, being $\hat{\mathrm{u}}$ and $\hat{\mathrm{v}}$ (or E_u and E_v), respectively. [see the framework of coordinates in Fig. 1(a)]. The 3-D cell architecture is quite beneficial for the independent manipulation of each of the $\hat{\mathrm{u}}$ and $\hat{\mathrm{v}}$ components. For instance, lateral slits, shown in Fig. 1(b), manipulate the $\hat{\mathrm{u}}$ component of the incident wave only, whereas the top/bottom slits, in Fig. 1(c), control the corresponding $\hat{\mathrm{v}}$ component. This allows splitting the problem into two independent subproblems, addressed hereafter in terms of two individual CMs.

A. Equivalent-Circuit Proposal and Characterization

The subproblem division mentioned above guarantees an individual treatment of the physical phenomenology associated with each of the components. This will be done via CMs, whose topology is the one depicted in Fig. 2. This topology has not been proposed before, according to the authors' point of view. The transmission line (TL) with characteristic impedance (CI) Z_0 describes the propagation of the incident wave. Both TLs having Z_1 and Z_2 as CIs denote the propagating TEM waves inside each of the slits in the *propagating region*. The TL lengths coincide with their corresponding slit lengths d_1 and d_2. For this case, two slits have been assumed on the walls. In the case of more than two slits, more TLs must be incorporated into the CM. The capacitances at the beginning of the TLs C_1 and C_2 account for the fringe fields at the discontinuity. Finally, the coupling between the *propagating and waveguide regions* is realized via transformers with turn ratios N_1 and N_2, describing how each of the TEM modes traveling along the TLs couple to the fundamental mode (TE_{10}) of the waveguide. This mode, though evanescent, is represented by a TL with CI Z_{10}^{TE} [40] and terminated by a short circuit, which emulates the effect of the ground plane. The presence of the TE_{10} mode is, from the circuit point of view, that of a conventional reactive load. Thus, in reflective structures, this type of load usually shifts the phase of the reflection coefficient.

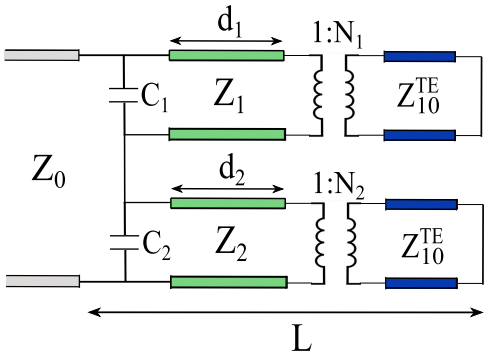

Fig. 2. Equivalent circuit of the proposed cell with a double slit.

Some of the circuit parameters are directly related to the cell geometry, as the lengths d_1, d_2, and L. Likewise, the CI of the incident wave coincides with that of free space $Z_0 = 376.73\ \Omega$. The CI of the TE_{10} mode in a regular waveguide is found in microwave textbooks and manuals [41]

$$Z_{10}^{\mathrm{TE}} = \frac{\eta_0 \omega}{c\sqrt{(\omega/c)^2 - (\pi/a)^2}}\,\Omega\,. \tag{1}$$

Otherwise, the remaining parameters $Z_{1/2}, C_{1/2}$, and $N_{1/2}$ must numerically be evaluated.

CST Microwave Studio software [43] has been employed for the numerical evaluation of these unknown parameters. For this, a simpler scenario is regarded, consisting of a single-slit cell excited by a plane wave impinging normally (e.g., a wave with the electric-field vector directed along the $\hat{\mathrm{u}}$-direction). A sketch of the cell and its corresponding CM are visible in the inset of Fig. 3(a). The simulation in CST is realized by imposing *unit-cell* boundary conditions on the cell and feeding it by *Floquet ports*. The S_{11} parameter provided by *CST* is mathematically manipulated. With the aid of the CM, Z, C, and N are obtained. Fig. 3(a)–(c) shows the evolution of this set of parameters with respect to w/p. As expected, the capacitance decreases as the slit width increases. The inverse behavior is otherwise observed for the CI and the transformer, denoting a sort of logarithmic trend. These values will henceforth be employed in the equivalent circuit in Fig. 2 and will be used to design the desired resonant behavior in Section II-B. To obtain the fittings of each plot in Fig. 3, the conftool of MATLAB has been used. In the case of Fig. 3(a), the trend of the plot is well fitted by the function in (2). Similarly, fittings have been conducted for the curves depicted in Fig. 3(c) by (3) and Fig. 3(b) by (4). The fitting values a and b can be seen in Table I

$$C = \mathrm{a}e^{b\frac{w}{p}} \tag{2}$$

$$N = a\log\left(b\frac{w}{p}\right) \tag{3}$$

$$Z = a\log\left(1 + b\frac{w}{p}\right). \tag{4}$$

B. Double-Symmetric Slit and Double-Asymmetric Slit Phase Resonance

This section is intended to validate the CM and describe the rich phenomenology of the cell. Two cell architectures will be used for this purpose. A first architecture consists of a cell with two identical slits on its walls. In the second cell type, both slits are geometrically different. The cells are fed by a plane wave with $\hat{\mathrm{u}}$

TABLE I
VALUES OF THE PARAMETERS FOR THE C, N, AND Z FITTINGS

Parameter	N fitting	Z fitting	C fitting
a	0.1341 ± 0.0152	192.4 ± 23.5	0.0401 ± 0.0043
b	27.87 ± 6.01	3.788 ± 0.656	-2.961 ± 0.501
r^2	0.99	0.999	0.98

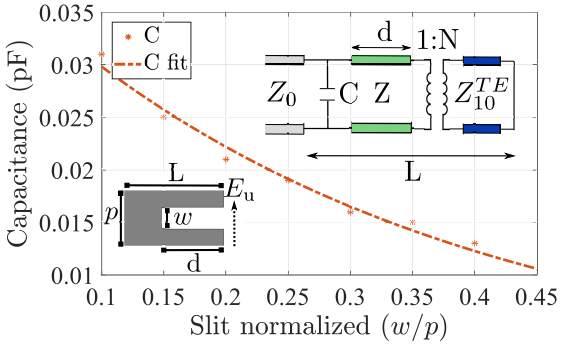

(a)

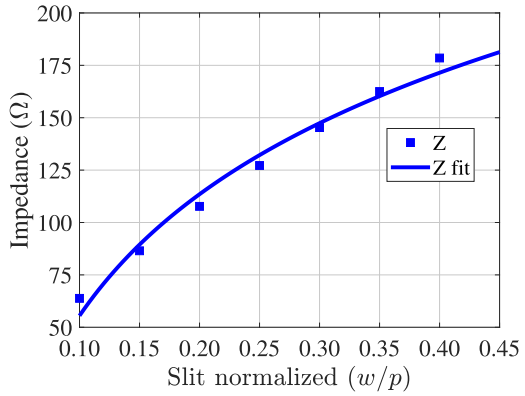

(b)

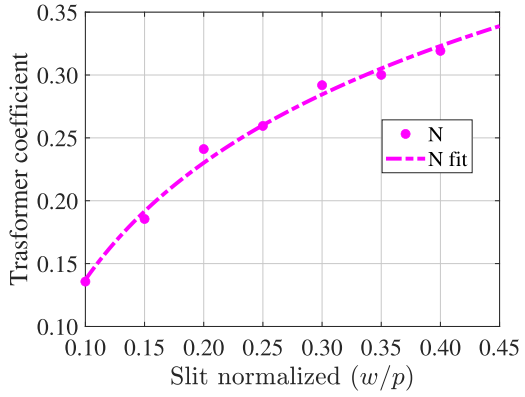

(c)

Fig. 3. Impedance, capacitance, and transformer coefficient versus normalized slit. (a) Capacitance. (b) Impedance. (c) Transformer. Fixed parameters: $L = 20$ mm, $d = 14$ mm, and $p = 10$ mm.

polarization. Of course, the concluding remarks can be applied for the $\hat{\mathrm{v}}$-component. The value of the circuit elements $Z_{1/2}$, $C_{1/2}$, $N_{1/2}$ of each individual TL have been taken from Fig. 3 and (2)–(4) as if the TLs were isolated. This constitutes an approximation in our model. However, as shown in Fig. 4, the agreement is excellent.

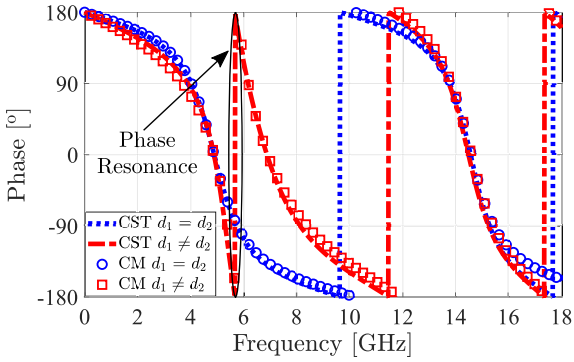

Fig. 4. Phase evolution of the reflection coefficient with respect to the frequency. Two cell architectures are considered. Common structure parameters: $p = 10$ mm and $L = 20$ mm. Parameters in identical double-slit case: $d_1 = d2 = 14.3$ mm and $w_1 = w_2 = 2$ mm. Parameters in different double-slit case: $d_1 = 14.3$ mm, $d_2 = 9.8$ mm, and $w_1 = w_2 = 2$ mm. Circuit parameters for both cases: $Z_1 = Z_2 = 105\ \Omega$, $C_1 = C_2 = 0.021$ pF, and $N_1 = N_2 = 0.25$.

In the case of identical slits ($d_1 = d_2 = 14.3$ mm), the phase behavior illustrated in Fig. 4 (blue color) emulates the behavior of a shorted TL: it goes from 180° at lower frequencies to 0° at wavelength values close to $d_i = \lambda/4$. After that it comes back to 180° at frequencies close to $d_i = \lambda/2$ ($i = 1, 2$). For the case with different slits ($d_1 \neq d_2$, red color), a sudden 180° resonance is manifested around 6 GHz. This resonance appears between 5 GHz, associated with $d_1 = 14.3$ mm $\approx \lambda/4$, and 7 GHz, associated with $d_2 = 9.8$ mm $\approx \lambda/4$. This is the so-called phase resonance, manifested as the mutual resonance between different slits. The CM performance is good enough to reproduce this kind of complex phenomenon, giving consistency to the proposal and becoming an efficient design tool for applications involving phase control. Phase control in terms of phase resonance is actually a novelty of this work, since it has not been employed before for this purpose to the author's knowledge.

III. DESIGN GUIDELINES. EXPERIMENTAL VALIDATION OF AN ULTRAWIDEBAND ROTATOR

This section will outline a set of design guidelines to be employed for the conception of an ultrawideband polarizer, especially a linear-to-linear field conversion from $\hat{\mathbf{y}}$ to $\hat{\mathbf{x}}$. As will be shown, the multiresonant phase behavior related to the cell is advantageous to achieve wideband conversions. The prototype here reported will cover a frequency band from 5.70 to 33.5 GHz, reporting a fractional bandwidth of 141.8%. The incident electric field, directed along $\hat{\mathrm{y}}$, is split into $\hat{\mathrm{u}}/\hat{\mathrm{v}}$ components. Optimal rotation from $\hat{\mathbf{y}}$ to $\mathbf{x}$ is achieved when $\mathrm{phase}(E_\mathrm{u}) - \mathrm{phase}(E_\mathrm{v}) = 180°$ [42]. The periodicity of the cell is 5 mm to avoid grating-lobes excitation. The metal thickness is 0.5 mm ($a = 4$ mm). In this scenario, the TE_{10} mode cut-off frequency in the waveguide region is around 37.5 GHz, being evanescent along the whole operation band. The TE_{10} impedance in the CMs keeps reactive.

A. Design Guidelines

For this functionality, a proper cell is that sketched in Fig. 5(a), containing four slits on the lateral walls and a single slit on the top/bottom ones. No phase resonance is induced for the $\hat{\mathbf{v}}$-polarization since it is controlled by a single slit. Otherwise, for $\hat{\mathbf{u}}$-polarization, controlled by the four slits on the lateral walls, the phase response does exhibit phase resonance, since the slit lengths are different ($d_{1\mathrm{u}} = d_{4\mathrm{u}} = 6.94$ mm and $d_{2\mathrm{u}} = d_{3\mathrm{u}} = 3.14$ mm). To see

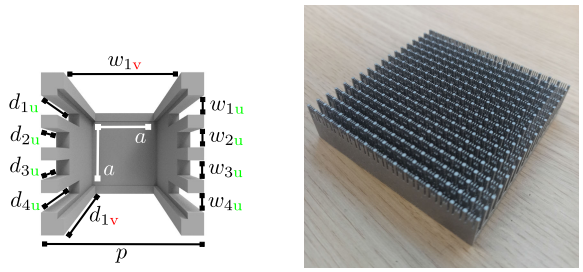

(a) (b)

Fig. 5. (a) Cell of the prototype. It includes just a single slit on the top/bottom walls, but four slits on the lateral walls. (b) Photograph of the whole prototype, being a 14 × 14-cell array.

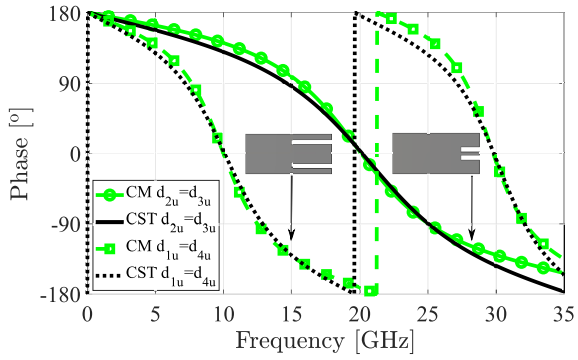

Fig. 6. Phase behavior of the reflection coefficient for û component for long and short slits individually.

that clearly, Fig. 6 shows the independent evolution of the phase of the reflection coefficient for a cell containing just the longest slits d_{1u}, d_{4u}, and for a cell including the shortest ones d_{2u}, d_{3u} only. A drawing of both cells appears in the insets of Fig. 6. The curve related to the longest slits crosses 0° at 10 GHz, whereas that for the shortest ones does it at 20 GHz. It is then expected that for the whole cell, shown in Fig. 5(a), phase resonance will appear at an intermediate frequency. This can be corroborated in Fig. 7 by an abrupt 180° jump at 15 GHz in the green curve, associated with the $\hat{\mathbf{u}}$ component. The same phenomenon is manifested at 25 GHz between a 0°-crossing of the shortest and longest slits.

The phase evolution of the $\hat{\mathbf{v}}$ (red curve in Fig. 7) component is designed to be shifted 180° with respect to $\hat{\mathbf{u}}$. A single slit is more appropriate to gain mechanical robustness. It has a length of $d_{1v} = 15$ mm, which introduces 0° and 180° at the frequency points where the opposite polarization has 180° and 0°, respectively. This fact satisfies the 180° phase shift between both components along the whole band, as shown by the black curve in Fig. 7. The reconstruction of the reflected components $\mathbf{u}$ and $\mathbf{v}$ results in a full power transfer to the $\hat{\mathbf{x}}$ component, as can be both checked theoretically and experimentally (thanks to the setup presented in Fig. 8) in Fig. 9.

B. Experimental Validation

Experimental results are plotted in Figs. 7 and 9. The prototype, shown in Fig. 5(b), was manufactured in a monolithic aluminum piece by means of *laser powder bed fusion* (LPBF) [44]. The experimental setup is mounted on a quasi-optical (QO) table. It consists of a horn feeding the rotator (DUT), as can be observed in Fig. 8. A commercial concave lens is placed at the focal distance with respect to the horn position to create a plane wave to illuminate the prototype. Different horn types were employed to cover the whole frequency

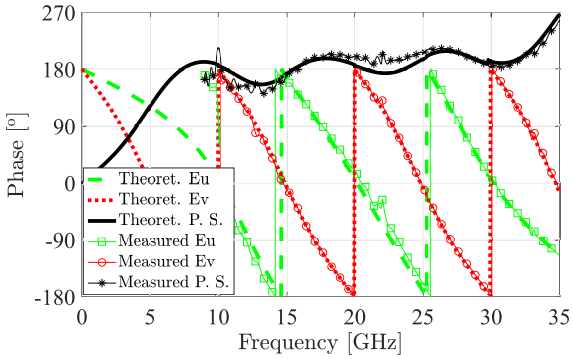

Fig. 7. Phase evolution of the reflection coefficient for both û and v̂ components separately. The figure also includes the phase shift along the whole band. Structure parameters: $p = 5$ mm, $a = 4$ mm, $L = 15$ mm, $d_{1u} = d_{4u} = 6.94$ mm, $d_{2u} = d_{3u} = 3.16$ mm, $d_{1v} = 15$ mm, $w_{1u} = w_{2u} = w_{3u} = w_{4u} = 0.6$ mm, and $w_{1v} = 3.6$ mm.

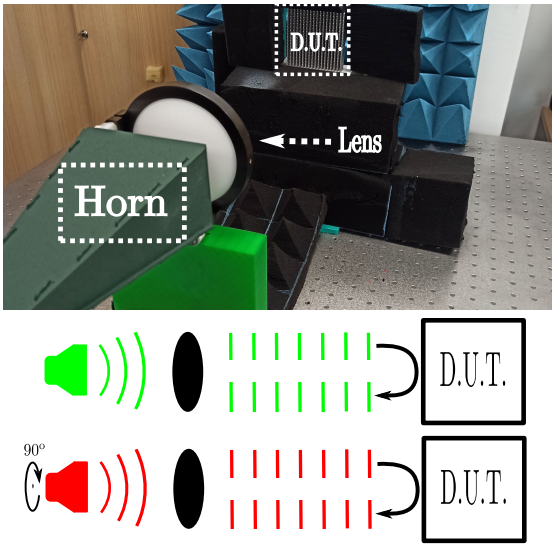

Fig. 8. Experimental setup. The photograph shows the QO table and the rest of the elements. The drawing describes schematically the measurement process. Each polarization is measured by the same horn, but with a different rotation along its axis.

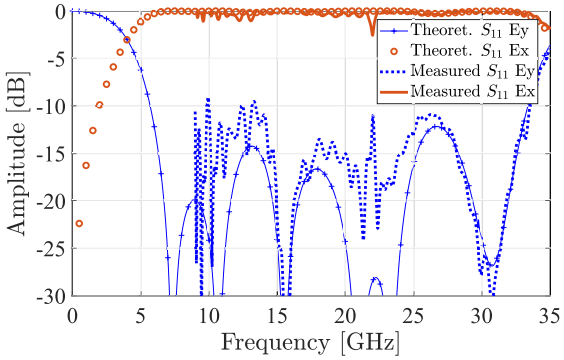

Fig. 9. Reflection-coefficient evolution for the copolarized field component E_y and the cross-polarized field component E_x. Structure parameters: $p = 5$ mm, $a = 4$ mm, $L = 15$ mm, $d_{1u} = d_{4u} = 6.94$ mm, $d_{2u} = d_{3u} = 3.16$ mm, $d_{1v} = 15$ mm, $w_{1u} = w_{2u} = w_{3u} = w_{4u} = 0.6$ mm, and $w_{1v} = 3.6$ mm.

band: WR-75 from 9 to 15 GHz; WR-51 from 15 to 22 GHz; WR-34 from 22 to 33 GHz; WR-28 from 33 to 40 GHz. Measurements from 5 to 9 GHz could not be done due to setup limitations. However, the agreement between the experimental results and those predicted

TABLE II
COMPARISON AMONG ROTATORS IN THE LITERATURE. FBW IS THE MEASURED FRACTIONAL BANDWIDTH. THE PARENTHESIS INDICATES THE PREDICTED BANDWIDTH

Ref.	Cell dimensions ($cell\ size \times thickness$)	FBW (%)	Full metal	Range (GHz)	Geom.
[16]	$0.54\lambda_m \times 0.54\lambda_m \times 0.43\lambda_m$	121	No	$5.4 - 22$	2D
[17]	$0.72\lambda_m \times 0.72\lambda_m \times 0.27\lambda_m$	97.78 (111.5)	No	$16.2 - 57$	2D
[18]	$0.77\lambda_m \times 0.77\lambda_m \times 0.22\lambda_m$	87.7	No	$6.67 - 17.1$	2D
[19]	$0.69\lambda_m \times 0.69\lambda_m \times 0.22\lambda_m$	95.2	No	$8.77 - 24.71$	2D
This work	$0.33\lambda_m \times 0.33\lambda_m \times 0.98\lambda_m$	116.8 (141.8)	Yes	$5.7 - 33.5$	3D

theoretically by CST and the CM is quite good in the experimental frequency range. It is true that small disagreement is appreciated between both sets of results, mainly due to fabrication inaccuracies and limitations on the setup. However, the predicted field rotation is exhibited, validating the CM and design guidelines here reported. To the authors' knowledge, this is the first ultrawideband rotator realized in a full-metal structure, covering a bandwidth of 141.8%.

Table II shows a comparison with other rotators reported in the literature. Since all the models referenced in the table are metallo-dielectric prototypes, the parameter λ_m refers to the wavelength at the central frequency in the dielectric

$$\lambda_m = \frac{2c}{(f_{\max} + f_{\min})\sqrt{\varepsilon_r}} \tag{5}$$

where $f_{\max}$ and $f_{\min}$ are the frequencies whose S_{11} is below -10 dB. The bandwidth obtained by the structure here presented is the longest one. It should be reminded that though the bandwidth predicted theoretically is about 141.8%, our experimental setup is not prepared to measure under 9 GHz. Thus, the experimental bandwidth is about 116.8% in the laboratory, which is still longer than most of the rotators in Table I. The full metal character makes our prototype to become a potential candidate for field-rotation functionalities, as well as other functionalities involving polarization control for scenarios under extreme conditions, such as space.

IV. CONCLUSION

The present manuscript presents a novel full-metal 3-D cell whose interesting properties have deeply been studied. Thanks to the individual control of the phase per polarization, in terms of the cell geometry, several functionalities involving polarization conversion are easily achieved. A field rotator exhibiting ultrawideband response has been successfully attained. The unit cell has been fully characterized using CMs, proving to be a very effective tool for the design. 3-D printing techniques based on LPBF have been used for the fabrication process. The experimental test has validated the prototype to become a candidate for this kind of functionalities in the range of microwaves and millimeter waves.

ACKNOWLEDGMENT

The authors would like to acknowledge the Advanced Center for Aerospace Technologies FADA-CATEC as the manufacturer of the prototype. The BBVA Foundation accepts no responsibility for the opinions, statements, and contents included in the project and/or the results thereof, which are entirely the responsibility of the authors.

REFERENCES

[1] S. Dang, O. Amin, B. Shihada, and M.-S. Alouini, "What should 6G be?" *Nature Electron.*, vol. 3, no. 1, pp. 20–29, Jan. 2020.

[2] J. Lundgren, O. Zetterstrom, F. Mesa, N. J. G. Fonseca, and O. Quevedo-Teruel, "Fully metallic dual-band linear-to-circular polarizer for K/Ka-band," *IEEE Antennas Wireless Propag. Lett.*, vol. 20, no. 11, pp. 2191–2195, Nov. 2021.

[3] K. X. Wang and H. Wong, "A wideband millimeter-wave circularly polarized antenna with 3-D printed polarizer," *IEEE Trans. Antennas Propag.*, vol. 65, no. 3, pp. 1038–1046, Mar. 2017.

[4] D. S. Kliger, J. W. Lewis, and C. E. Randall, *Polarized Light in Optics and Spectroscopy*. New York, NY, USA: Academic, 1990.

[5] Y. Jia, Y. Liu, Y. J. Guo, K. Li, and S.-X. Gong, "Broadband polarization rotation reflective surfaces and their applications to RCS reduction," *IEEE Trans. Antennas Propag.*, vol. 64, no. 1, pp. 179–188, Jan. 2016.

[6] P. Su, Y. Zhao, S. Jia, W. Shi, and H. Wang, "An ultra-wideband and polarization-independent metasurface for RCS reduction," *Sci. Rep.*, vol. 6, p. 20387, Feb. 2016.

[7] Y. Liu, K. Li, Y. Jia, Y. Hao, S. Gong, and Y. J. Guo, "Wideband RCS reduction of a slot array antenna using polarization conversion metasurfaces," *IEEE Trans. Antennas Propag.*, vol. 64, no. 1, pp. 326–331, Jan. 2016.

[8] M. Barkabian, N. Sharifi, and N. Granpayeh, "Multi-functional high-efficiency reflective polarization converter based on an ultra-thin graphene metasurface in the THz band," *Opt. Exp.*, vol. 29, pp. 20160–20174, 2021.

[9] F. Zeng, L. Ye, L. Li, Z. Wang, W. Zhao, and Y. Zhang, "Tunable mid-infrared dual-band and broadband cross-polarization converters based on U-shaped graphene metamaterials," *Opt. Exp.*, vol. 27, pp. 33826–33839, 2019.

[10] R. C. Tyan et al., "Design, fabrication, and characterization of form-birefringent multilayer polarizing beam splitter," *J. Opt. Soc. Amer. A, Opt. Image Sci.*, vol. 14, no. 7, pp. 1627–1636, 1997.

[11] N. Hill and S. Cornbleet, "Microwave transmission through a series of inclined gratings," *Proc. Inst. Elect. Eng.*, vol. 120, no. 4, pp. 407–412, Apr. 1973.

[12] N. Amitay and A. A. M. Saleh, "Broad-band wide-angle quasi-optical polarization rotators," *IEEE Trans. Antennas Propag.*, vol. AP-31, no. 1, pp. 73–76, Jan. 1983.

[13] P. Fei et al., "Versatile cross-polarization conversion chiral metasurface for linear and circular polarizations," *Adv. Opt. Mater.*, vol. 8, no. 13, Jul. 2020, Art. no. 2000194.

[14] J. Y. Dai et al., "Wireless communication based on information metasurfaces," *IEEE Trans. Microw. Theory Techn.*, vol. 69, no. 3, pp. 1493–1510, Mar. 2021.

[15] M. I. Khan, Q. Fraz, and F. A. Tahir, "Ultra-wideband cross polarization conversion metasurface insensitive to incidence angle," *J. Appl. Phys.*, vol. 121, no. 4, Jan. 2017, Art. no. 045103.

[16] M. S. J. Moghadan, M. Akbari, F. Samadi, and A. R. Sebak, "Wideband cross polarization rotation based on reflective anisotropic surfaces," *IEEE Access*, vol. 6, pp. 15919–15925, 2018.

[17] A. A. Omar, W. Hong, A. Al-Awamry, and A.-E. Mahmoud, "A single-layer vialess wideband reflective polarization rotator utilizing perforated holes," *IEEE Antennas Wireless Propag. Lett.*, vol. 19, no. 12, pp. 2053–2056, Dec. 2020.

[18] J. Xu, R. Li, S. Wang, and T. Han, "Ultra-broadband linear polarization converter based on anisotropic metasurface," *Opt. Exp.*, vol. 26, no. 20, pp. 26235–26241, Oct. 2018.

[19] B. Lin et al., "Ultra-wideband and high-efficiency reflective polarization converter for both linear and circular polarized waves," *Appl. Phys. A, Solids Surf.*, vol. 125, no. 2, pp. 1–8, Feb. 2019.

[20] C. Huang, Y. Feng, J. Zhao, Z. Wang, and T. Jiang, "Asymmetric electromagnetic wave transmission of linear polarization via polarization conversion through chiral metamaterial structures," *Phys. Rev. B, Condens. Matter*, vol. 85, no. 19, May 2012, Art. no. 195131.

[21] Y. Ye and S. He, "90° polarization rotator using a bilayered chiral metamaterial with giant optical activity," *Appl. Phys. Lett.*, vol. 96, no. 20, May 2010, Art. no. 203501.

[22] A. K. Rashid, B. Li, and Z. Shen, "An overview of three-dimensional frequency-selective structures," *IEEE Antennas Propag. Mag.*, vol. 56, no. 3, pp. 43–67, Jun. 2014.

[23] A. Sadeqi, H. Rezaei-Nejad, R. E. Owyeung, and S. Sonkusale, "Three dimensional printing of metamaterial embedded geometrical optics (MEGO)," *Microsyst. Nanoeng.*, vol. 5, no. 1, p. 16, 2019.

[24] M. Harnois, M. Himdi, W. Y. Yong, S. K. A. Rahim, K. Tekkouk, and N. Cheval, "An improved fabrication technique for the 3-D frequency selective surface based on water transfer printing technology," *Sci. Rep.*, vol. 10, no. 1, p. 1714, Feb. 2020.

[25] A. A. Omar and Z. Shen, "Thin 3-D bandpass frequency-selective structure based on folded substrate for conformal radome applications," *IEEE Trans. Antennas Propag.*, vol. 67, no. 1, pp. 282–290, Jan. 2019.

[26] A. A. Omar, J. Kim, and W. Hong, "A 3-D lumped-components-free absorptive frequency-selective transmission structure featuring very wide two-sided absorption bandwidths," *IEEE Antennas Wireless Propag. Lett.*, vol. 19, no. 5, pp. 761–765, May 2020.

[27] X.-J. Huang, C. Yang, Z.-H. Lu, and P.-G. Liu, "A novel frequency selective structure with quasi-elliptic bandpass response," *IEEE Antennas Wireless Propag. Lett.*, vol. 11, pp. 1497–1500, 2012.

[28] C. Molero and M. García-Vigueras, "Circuit modeling of 3-D cells to design versatile full-metal polarizers," *IEEE Trans. Microw. Theory Techn.*, vol. 67, no. 4, pp. 1357–1369, Apr. 2019.

[29] C. M. Jimenez, E. Menargues, and M. García-Vigueras, "All-metal 3-D frequency-selective surface with versatile dual-band polarization conversion," *IEEE Trans. Antennas Propag.*, vol. 68, no. 7, pp. 5431–5441, Jul. 2020.

[30] X. Wang, Y. Cheng, and Y. Dong, "Millimeter-wave dual-polarized metal transmitarray antenna with wide gain bandwidth," *IEEE Antennas Wireless Propag. Lett.*, vol. 21, no. 2, pp. 381–385, Feb. 2022.

[31] C. Molero, H. Legay, T. Pierré, and M. García-Vigueras, "Broadband 3D-printed polarizer based on metallic transverse electro-magnetic unit-cells," *IEEE Trans. Antennas Propag.*, vol. 70, no. 6, pp. 4632–4644, Jun. 2022.

[32] N. Chahat, B. Cook, H. Lim, and P. Estabrook, "All-metal dual-frequency RHCP high-gain antenna for a potential Europa Lander," *IEEE Trans. Antennas Propag.*, vol. 66, no. 12, pp. 6791–6798, Dec. 2018.

[33] S. I. Grosz, D. C. Skigin, and A. N. Fantino, "Resonant effects in compound diffraction gratings: Influence of the geometrical parameters of the surface," *Phys. Rev. E, Stat. Phys. Plasmas Fluids Relat. Interdiscip. Top.*, vol. 65, no. 5, May 2002, Art. no. 056619.

[34] D. C. Skigin and R. A. Depine, "Transmission resonances of metallic compound gratings with subwavelength slits," *Phys. Rev. Lett.*, vol. 95, no. 21, Nov. 2005, Art. no. 217402.

[35] Y. Jiang, L. Wang, J. Wang, C. N. Akwuruoha, and W. Cao, "Ultra-wideband high-efficiency reflective linear-to-circular polarisation converter based on metasurface at terahertz frequencies," *Opt. Exp.*, vol. 25, pp. 27616–27623, Oct. 2017.

[36] A. P. Hibbins, I. R. Hooper, M. I. Lockyear, and J. R. Sambles, "Microwave transmission of a compound gratings," *Phys. Rev. Lett.*, vol. 96, Jun. 2006, Art. no. 257402.

[37] D. C. Skigin, V. V. Veremey, and R. Mittra, "Superdirective radiation from finite gratings of rectangular grooves," *IEEE Trans. Antennas Propag.*, vol. 47, no. 2, pp. 376–383, Feb. 1999.

[38] F. Medina, F. Mesa, and D. C. Skigin, "Extraordinary transmission through arrays of slits: A circuit theory model," *IEEE Trans. Microw. Theory Techn.*, vol. 58, no. 1, pp. 105–115, Jan. 2010.

[39] C. Molero, R. Rodríguez-Berral, F. Mesa, and F. Medina, "Dynamical equivalent circuit for 1-D periodic compound gratings," *IEEE Trans. Microw. Theory Techn.*, vol. 64, no. 4, pp. 1195–1208, Apr. 2016.

[40] A. Alex-Amor, F. Mesa, Á. Palomares-Caballero, C. Molero, and P. Padilla, "Exploring the potential of the multi-modal equivalent circuit approach for stacks of 2-D aperture arrays," *IEEE Trans. Antennas Propag.*, vol. 69, no. 10, pp. 6453–6467, Oct. 2021.

[41] D. M. Pozar, *Microwave Engineering*. 4th ed. New York, NY, USA: Wiley, 2012.

[42] B. Kamal, J. Chen, Y. Yingzeng, J. Ren, S. Ullah, and W. U. R. Khan, "High efficiency and ultra-wideband polarization converter based on an L-shaped metasurface," *Opt. Mater. Exp.*, vol. 11, no. 5, pp. 1343–1352, 2021.

[43] Dassault Systèmes. *CST Microwave Studio*. [Online]. Available: https://www.3ds.com/products-services/simulia/products/cststudio-suite/solvers/

[44] S. L. Sing and W. Y. Yeong, "Laser powder bed fusion for metal additive manufacturing: Perspectives on recent developments," *Virtual Phys. Prototyping*, vol. 15, no. 3, pp. 359–370, Jun. 2020.